J Mater Sci (2017) 52:489–503

Hydrothermal growth of one-dimensional Ce-doped TiO_2 nanostructures for solid-state DSSCs comprising Mg-doped $CuCrO_2$

Morteza Asemi[1,2] and Majid Ghanaatshoar[1,2,*]

[1] *Laser and Plasma Research Institute, Shahid Beheshti University, G.C., Evin, 1983969411 Tehran, Iran*
[2] *Solar Cells Research Group, Shahid Beheshti University, G.C., Evin, 1983969411 Tehran, Iran*

Received: 10 May 2016
Accepted: 26 August 2016
Published online: 7 September 2016

ABSTRACT

In this work, hydrothermal method was used to grow the one-dimensional Ce-doped TiO_2 nanostructures on the fluorine-doped tin oxide glass. The incorporation of cerium atoms into the TiO_2 lattice was investigated by structural and electrical analyses. The results showed that TiO_2 nanorod arrays had maximum electrical conductivity for 3 % of Ce dopant. The increase in the electrical conductivity can be ascribed to the formation of oxygen vacancy in TiO_2 nanostructures with Ce doping. The morphology of the as-grown nanorods revealed that the diameter of the TiO_2 nanorods increased with Ce doping concentration. Hydrothermal etching treatment was performed on the as-grown 3 % Ce-doped TiO_2 nanorod arrays in hydrochloric acid solution at 160 °C for different time durations. The obtained results clearly showed that the morphology change from the nanorods to the nanotubes occurred after 4 h of etching during hydrothermal treatment. In addition, sol–gel process was employed to synthesize 5 % Mg-doped $CuCrO_2$ nanoparticles with p-type conductivity as solid-state electrolyte. The solid-state DSSCs fabricated using hydrothermally treated 3 % Ce-doped TiO_2 nanorods displayed better photovoltaic performance than those made from the untreated ones. This is attributed to the larger specific surface of the hydrothermally treated nanorods compared with the untreated ones. The dye-loading measurement confirmed that the amounts of adsorbed dye on the surface of hydrothermally treated nanorods were higher than that of the untreated ones.

Introduction

Among the different n-type semiconductors, titanium dioxide (TiO_2) has been recognized as one of the most promising materials for use in photocatalysts, dye-sensitized solar cells (DSSCs), lithium-ion batteries, and gas sensors due to its unique physical, optical, and chemical properties such as wide bandgap, good photocatalytic activity, chemical stability, and non-toxicity [1–3]. In addition, vertically aligned one-

Address correspondence to E-mail: m-ghanaat@sbu.ac.ir

DOI 10.1007/s10853-016-0348-z

dimensional (1D) titanium dioxide nanostructures such as nanowires, nanorods, and nanotubes as photoanodes in DSSCs have received a great deal of attention because of their large surface area, high crystallinity, and excellent charge transport properties which effectively suppress the charge recombination at grain boundaries [4, 5]. Until now, 1D vertically aligned TiO_2 nanostructures have been grown by different methods. Wei et al. reported the growth of dense and vertically aligned TiO_2 nanowires on titanium substrate by direct oxidation of titanium foils [6]. Shankar et al. prepared highly ordered TiO_2 nanotube arrays by electrochemical anodization of Ti foils [7]. Foong et al. synthesized vertically aligned TiO_2 nanotube arrays by liquid-phase atomic layer deposition in nanoporous anodic alumina templates [8]. The growth of TiO_2 nanorods on a tantalum substrate by metal–organic chemical vapor deposition was also reported by Chen et al. [9]. Furthermore, single-crystalline rutile TiO_2 nanorod arrays on different substrates by hydrothermal method were recently reported [10]. In comparison with the other methods, the hydrothermal method has been identified as one of the simple, low-cost, and low-temperature techniques to grow the nanostructures [11]. Although, 1D TiO_2 nanostructures have been extensively investigated but the growth of TiO_2 nanorod arrays on fluorine-doped tin oxide conductive glass (FTO) substrates via hydrothermal method has just recently been reported [12].

DSSCs have been considered as an important alternative to conventional Si-based solar cells, because of their high-energy conversion efficiency (>13 %), facile fabrication process, and low manufacturing cost [13–15]. However, major problems, such as leakage or evaporation of liquid electrolyte have limited the long-term operation and practical use of DSSCs [16]. To overcome these problems, considerable attempts have been made to substitute the liquid electrolyte with solid-state or gel-state electrolytes [17–19]. Unfortunately, the efficiency of fabricated solid-state DSSCs has been restricted due to pore-filling problems [20]. Pore-filling problems in solid-state DSSCs can be solved by one-dimensional TiO_2 nanorods/nanowires due to their direct pathways for penetration of solid-state electrolyte [21, 22]. Xu et al. fabricated high-efficiency solid-state DSSCs including TiO_2-coated ZnO nanowire arrays and spiro-OMeTAD as photoanode and solid-state electrolyte, respectively [23]. Roh et al. synthesized hierarchical anatase pine tree-like TiO_2 nanotubes by hydrothermal method for application in solid-state DSSCs [24]. Wang et al. fabricated solid-state DSSCs with ordered TiO_2 nanorods on FTO substrate as photoanodes [25]. In a previous work, the grown vertically aligned TiO_2 nanorods on FTO substrates were used as photoanode for fabrication of solid-state DSSCs comprising Zn-doped $CuCrO_2$ nanoparticles as solid-state electrolyte [26]. The use of TiO_2 nanorods instead of TiO_2 nanoparticles promoted the efficiency of fabricated solid-state DSSCs due to better penetration of solid-state electrolyte in space between nanorod arrays [27]. However, the efficiency improvement of fabricated devices was not significant due to insufficient dye adsorption on the surface of the nanorods [28, 29]. Vertically aligned TiO_2 nanotube arrays are superior to nanowires or nanorods because of their increased surface area for dye adsorption. Due to this reason, more efficient light harvesting for increasing the amount of photogenerated charge carriers can be occurred.

In the current work, we study the effect of Ce dopant concentration on structural properties of vertically aligned TiO_2 nanorod arrays. The growth of the TiO_2 nanorods on the FTO substrate is performed by hydrothermal method. The cerium is chosen as a dopant which can improve the n-type conductivity of the TiO_2 semiconductor through creation of oxygen vacancies [30–32]. It is well-known that the oxygen vacancies are the origin of the n-type conductivity in TiO_2 semiconductors [33, 34]. After preparation of Ce-doped TiO_2 nanorods, hydrothermal etching treatment is used for transforming them into Ce-doped TiO_2 nanotubes. We expect that the use of nanotubes instead of nanorods can improve the efficiency of constructed solid-state DSSCs as they have relatively higher surface area. Furthermore, in this way, a large amount of the solid-state electrolyte can fill into the space between TiO_2 nanostructures.

Experimental methods

The vertically aligned Ce-doped TiO_2 nanorod arrays were grown directly on fluorine-doped tin oxide (FTO) glass substrate by hydrothermal method. Firstly, FTO glass substrates ($1.5 \times 2.0\ cm^2$) were cleaned by ethanol and distilled water in an ultrasonic bath for 30 min to remove the possible impurities, were dried in air at 60 °C for 30 s and then

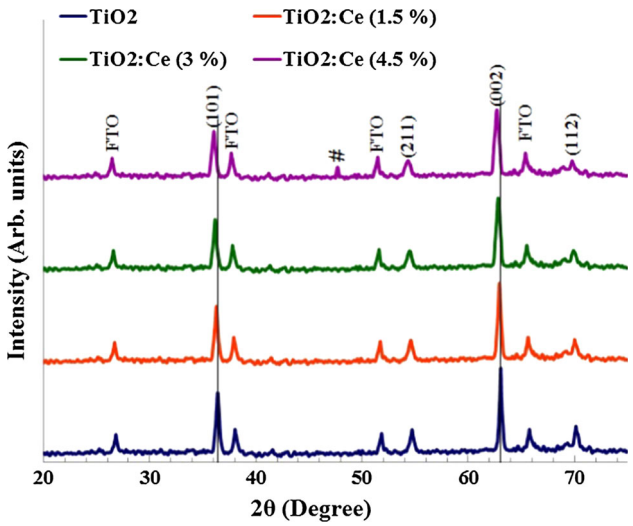

Figure 1 X-ray diffraction patterns of undoped and Ce-doped TiO_2 nanorod arrays on FTO glass substrates. Peaks labeled as # are attributed to the CeO_2 structure. The solid lines are guide for the eyes.

were put into a Teflon-lined stainless steel autoclave (100 ml volume). Then, 30 ml distilled water was mixed with 30 ml hydrochloric acid (HCl, Amertat Shimi Co., Iran) under magnetic stirring at room temperature. After stirring for 10 min, 1.1 ml titanium tetraisopropoxide (TTIP, Samchun Chemical Co., Korea) accompanied with different values of cerium (III) nitrate pentahydrate ($Ce(NO_3)_3{\cdot}5H_2O$, Chem-Lab NV Co., Belgium) as dopant source was added to the mentioned mixed solution and stirred vigorously for 20 min to obtain a clear and transparent solution. Afterwards, the resulting clear solution was transferred into the Teflon-lined stainless steel autoclave. The sealed autoclave was placed in a laboratory furnace (F35L-1200, Azar Furnace Co., Iran) at 160 °C for 12 h. At the end of the reaction, the autoclave was cooled down to room temperature naturally and the grown Ce-doped TiO_2 nanorod array on the FTO substrate was taken out, rinsed with distilled water and ethanol for several times to remove the residual reactants, and finally dried in air at 60 °C for 30 s. In order to convert the prepared nanorods to nanotubes, the as-grown TiO_2 nanorod arrays on FTO substrates were immersed in HCl (25 mL of 7 M aqueous solution) and hydrothermally treated at 160 °C for different time durations. The hydrothermally treated TiO_2 nanorods were rinsed with distilled water and ethanol for several times to remove the residual reactants, and finally dried in air at 60 °C for 30 s.

5 % Mg-doped $CuCrO_2$ nanoparticles were synthesized by sol–gel process. In this experiment, the solution was prepared by dissolving copper acetate monohydrate ($Cu(CH_3COO)_2{\cdot}H_2O$, Merck Co., Germany) and chromium nitrate nonahydrate ($Cr(NO_3)_3{\cdot}9H_2O$, Merck Co., Germany) as starting materials and magnesium nitrate hexahydrate ($Mg(NO_3)_2{\cdot}6H_2O$, Merck Co., Germany) as a dopant source in 2-methoxyethanol ($CH_3(CH_2)_2OOH$, Merck Co., Germany) at 60 °C for 3 h using a magnetic stirrer. The molar ratio of copper ions to the sum of chromium and magnesium was fixed at 1.0 and the concentration of copper ions in the solution was equal to 0.7 M. The resultant transparent and deep green solution was then heated up to 110 °C and kept at this temperature for 3 h. The dried powder was annealed in air in the laboratory furnace at 900 °C for 1 h. After annealing, the prepared particles were milled in a planetary ball-milling machine (NARYA MPM-2*250 H, Amin-Asia Co., Iran) at 400 rpm for 5 h in a zirconia vessel and with zirconia balls in ethanol to produce very fine particles. The weight ratio of ball to powder was 10:1.

The hydrothermally treated Ce-doped TiO_2 nanorod arrays on FTO glass were used as photoanode for DSSCs. Prior to dye sensitization, the hydrothermally treated Ce-doped TiO_2 nanorod arrays were heated up to 150 °C and kept at this temperature for 30 min. After cooling down to 80 °C, the Ce-doped TiO_2 electrodes were dipped into 0.5 mM solution of N719 dye (Dyesol Co., Australia) in ethanol for 24 h at room temperature and then washed with ethanol and dried in air. Subsequently, Mg-doped $CuCrO_2$ nanoparticles were ultrasonically dispersed in ethanol and deposited on the surface of the Ce-doped TiO_2 photoelectrode using a spin coater (SC-410 spincoater, Backer Viera Trading Co., Iran) at spin speed of 1000 rpm for 30 s. In addition, counter electrodes were prepared by spin-coating a 5 mM 2-propanol solution of H_2PtCl_6 on FTO substrate at 500 rpm for 10 s and followed by annealing at 450 °C for 30 min. The solid-state DSSCs were assembled in a sandwich configuration with prepared Ce-doped TiO_2 photoanode and platinum-coated FTO counter electrode. The active area of the DSSCs was 0.2 cm^2. Finally, to improve the interconnection between the nanoparticles and the penetration of a large amount of the nanoparticles into the photoanode, the constructed solid-state DSSCs were pressed by hydraulic press (769YP-15A, Tianjin Keqi High and New

Table 1 Lattice parameters of the as-grown undoped and Ce-doped TiO_2 nanorods

Lattice parameter	TiO_2	TiO_2:Ce (1.5 %)	TiO_2:Ce (3 %)	TiO_2:Ce (4.5 %)
a (Å)	4.595	4.599	4.605	4.611
c (Å)	2.956	2.959	2.962	2.967

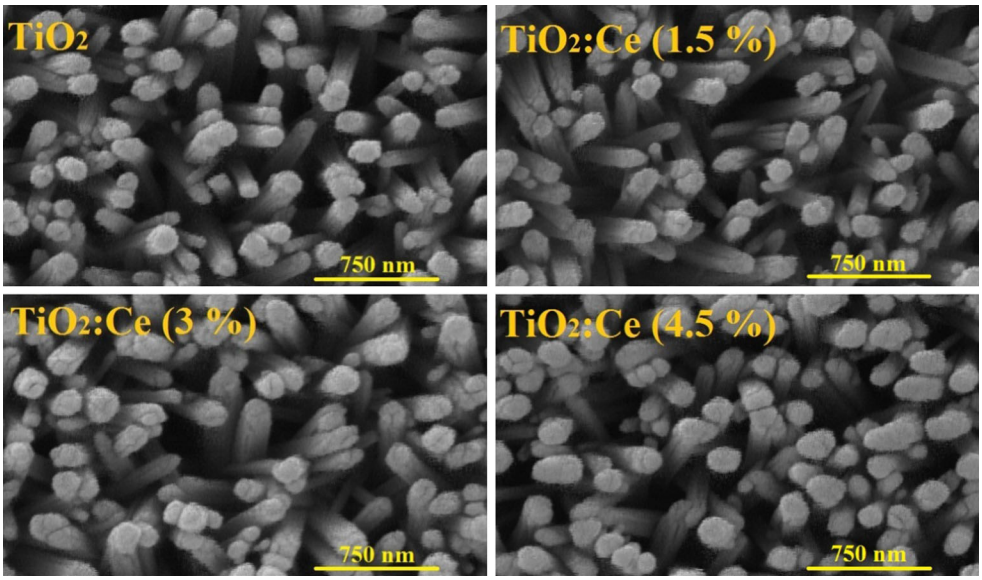

Figure 2 Top-view FE-SEM images of the as-grown undoped and Ce-doped TiO_2 nanorod arrays with 1.5, 3, and 4.5 % Ce doping concentration.

Technology Co., China) under constant pressure (5 MPa) at room temperature for 30 min.

The shape and surface morphology of the as-grown nanorods and Mg-doped $CuCrO_2$ nanoparticles were characterized by a Hitachi S-4100 field-emission scanning electron microscope and a Tescan mira 3 xmu, respectively. The length of the vertically aligned Ce-doped TiO_2 nanorods was also determined by cross-sectional field-emission scanning electron microscopy (FE-SEM). In addition, the transmission electron microscopy (TEM) was carried out using a Zeiss EM10C microscope operating with an accelerating voltage of 100 kV to estimate the size of the nanoparticles. The crystalline structure and growth orientation of the as-grown undoped and doped TiO_2 nanorods were also characterized by X-ray powder diffraction (XRD) analysis with Cu Kα radiation ($\lambda = 1.5406$ Å) in the Bragg angle ranging between 10° and 80°. The hot-probe and Hall effect measurements were carried out to study the electrical properties of the as-grown Ce-doped TiO_2 nanorods. The magnetic field in the Hall effect measurements was adjusted at 400 mT. The current density–voltage (J–V) characteristics were determined with a computer-controlled I–V tracer (IV-25, Sharif Solar, Iran) under the illumination of an AM1.5G solar simulator (SIM-1000, Sharif Solar, Iran) to determine the photovoltaic performance of the assembled DSSCs. The light intensity was adjusted to 100 mW/cm^2 using a reference Si solar cell. To estimate the amount of adsorbed N719 dye on the surface of the TiO_2 nanorod arrays, the sensitized Ce-doped TiO_2 photoanodes were immersed into 5 mL of 0.1 M NaOH aqueous solution to desorb dye molecules from the TiO_2 photoanodes. Then, a UV–Vis spectrophotometer (AvaSpec-3648, Avantes, Netherlands) was used to measure the UV–Vis absorption spectra of the resulting solutions. Photoluminescence (PL) spectra of the as-grown Ce-doped TiO_2 nanorods were determined by a fluorescence spectrophotometer (Cary Eclipse, Varian, Australia) using the 300-nm line of a Xe lamp as the excitation source at room temperature. In order to investigate the charge recombination rate in the prepared DSSCs, the open-circuit voltage decay experiment was carried out by recording the decay of the open-circuit voltage (V_{OC}) after turning off the illumination, at steady state.

Table 2 Electrical properties of the undoped and Ce-doped TiO_2 nanorods

Sample	TiO_2	TiO_2:Ce (1.5 %)	TiO_2:Ce (3 %)	TiO_2:Ce (4.5 %)
Charge carriers concentration (cm^{-3})	3.1×10^{17}	8.3×10^{17}	6.6×10^{18}	1.4×10^{18}
Hall mobility ($cm^2\ V^{-1}\ s^{-1}$)	5.3	5.1	4.6	4.2
Conductivity ($S\ cm^{-1}$)	0.26	0.68	4.8	0.94

Results and discussion

In order to study the effect of Ce dopant concentration on the crystalline structure of nanorods, X-ray diffraction measurements were first performed on the prepared nanorods. The XRD patterns of the as-grown undoped and Ce-doped TiO_2 nanorods in Fig. 1 exclusively show that the as-synthetized TiO_2 nanorods without annealing are in rutile phase (JCPDS card No. 00-001-1292) [35]. Previously, Liao et al. showed that the formation of anatase, rutile, and brookite phases of TiO_2 during the hydrothermal method strongly depends on the starting materials [36]. Using the distilled water, hydrochloric acid, and titanium tetraisopropoxide as the starting materials, the expected phase is pure rutile, in agreement with the experimental result of Liu et al. [12]. The obtained results also verify that up to 3 % of Ce-doped TiO_2, there is no trace of any secondary phase or clusters such as cerium oxide and binary titanium cerium phases, confirming the achievement of the single-phase as-grown TiO_2 nanorods. This signifies that the Ti ions are successfully replaced by Ce ions in the crystalline structure. Furthermore, the sharp and intense peaks in the XRD patterns indicate that the as-grown nanorods are highly crystalline but in polycrystalline phase. However with 4.5 % of Ce doping, the appearance of an extra peak at 47.44 can be attributed to the CeO_2 (JCPDS Card No. 00-002-1306) [37]. As can be seen from Fig. 1, as the cerium doping percentage increases, the position of the diffraction peaks shifts to lower angles, their intensity decreases, and the full-width at half-maximum (FWHM) of the TiO_2 diffraction peaks increases gradually. The observed decrease in the crystalline quality of the TiO_2 nanorods can be attributed to the formation of lattice disorder and strain induced by substitution of larger Ce^{4+} (0.96 Å) in the place of Ti^{4+} (0.60 Å) due to the increase of the lattice parameters [38]. This trend (the slight shift in the peak positions and the variation of the corresponding lattice constant) is consistent with the Vegard's law, which states that the lattice parameters of the $Ti_{1-x}Ce_xO_2$ ternary alloy can be linearly varied with Ce content from titanium oxide ($x = 0$) to cerium oxide ($x = 1$) [39]. The Lattice parameters of the as-grown nanorods obtained from the XRD patterns are presented in Table 1. Using Debye–Scherrer's equation [40],

$$d_{hkl} = \frac{0.9\lambda}{(\beta \cos(\theta))}.$$

in which, d_{hkl} represents the size of the crystallites, λ is the wavelength of the radiation (1.5406 Å), β is FWHM in radians and θ is half of the scattering angle, the size of the crystallites along (002) direction can be estimated to be about 30.1, 25.6, 20.3, and 16.7 nm for undoped, 1.5, 3, and 4.5 % Ce-doped TiO_2, respectively.

Due to the low solubility of the cerium ions in TiO_2, at higher levels of doping, only a few Ce^{4+} ions penetrate into the TiO_2 lattice and the segregation of the dopants at the grain boundaries prevents the crystallite growth during the synthesizing process. The decrease in the size of the TiO_2 crystallites with Ce doping is mainly attributed to this phenomenon. Our results are in agreement with the other literature studies [41, 42].

Figure 2 shows typical FE-SEM images of the as-grown crystalline rutile TiO_2 nanorod arrays on FTO substrates with different concentrations of the dopant. The surface morphology of the TiO_2 nanorods reveals that the entire surface of the FTO substrate is uniformly covered by highly ordered nanorods. Furthermore, as expected, the as-grown undoped and Ce-doped TiO_2 nanorods have tetragonal shape with square top facets due to the tetragonal crystal structure. Moreover, the cross-sectional FE-SEM images confirm that the as-grown nanorods are perpendicular to the substrate, and that there are no side branches. The top-view FE-SEM images show that the average area of the rectangular cross section of the synthesized nanorods gradually increases with

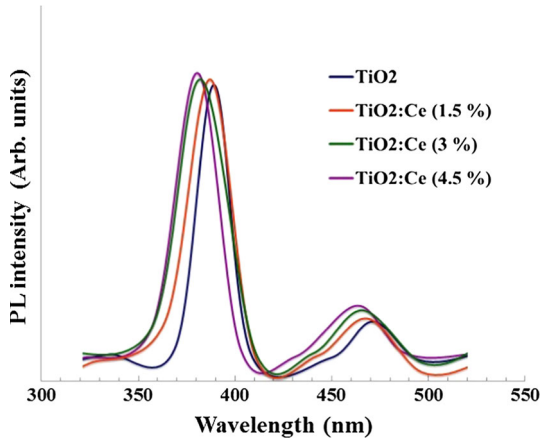

Figure 3 Photoluminescence spectra of Ce-doped TiO_2 nanorods.

the increasing concentration of the Ce dopant from 0 to 4.5 %. A similar trend in the diameter of the Fe-doped ZnO nanorods was observed by Xiao et al. [43]. The morphology changes of the one-dimensional ZnO nanostructures were elucidated by the dislocation-driven growth mechanism due to the variation of the initial solution concentration [44]. The increase in the diameter of the as-grown TiO_2 nanorod arrays with Ce doping can be understood by this growth mechanism. Cerium doping has a similar effect on the supersaturation level of the initial growth solutions.

In order to investigate the electrical properties (charge carrier concentration, mobility, and conductivity) of the as-grown undoped and Ce-doped TiO_2 nanorods, Hall effect measurement was performed. The electrical properties of the vertically aligned TiO_2 nanorods with different Ce doping concentrations have been tabulated in Table 2. Hot-probe measurement confirmed the n-type conductivity of the as-grown nanorods. The n-type conductivity of TiO_2 structure is mainly attributed to the donor-type defects such as titanium interstitials and oxygen vacancies [33, 34]. When TiO_2 is doped with an element which has a higher oxidation state than Ti^+ [4], the electrical conductivity improvement originates from the presence of excess free electrons [45]. On the other hand, the increase in the electrical conductivity of the doped TiO_2 with tri- or tetravalent metals is ascribed to the oxygen vacancies in the structures. Iwaszuk and Nolan showed that Ce doping decreases the formation energy of oxygen vacancies in TiO_2 [31]. Similar trend is obtained for Ce-doped TiO_2 structure by Albuquerque [32]. Their results indicate that the energy levels of oxygen vacancies in metal oxide semiconductors are affected by doping. In order to investigate the oxygen vacancy in the as-grown undoped and Ce-doped TiO_2 nanorods, the PL measurement was performed. Figure 3 shows the room temperature PL spectra of the as-grown nanorod arrays in the wavelength range of 320–520 nm. As can be seen from this figure, the nanorods exhibit two strong PL signals centered at approximately 370 and 470 nm. The first emission peak that appeared at ~370 nm (3.36 eV) is due to the emission of bandgap transition. The second emission peak around 470 nm (2.65 eV) results from the oxygen vacancies in TiO_2 structure [46], which are about 2.66 eV above the valence band and 0.7 eV below the conduction band of TiO_2. There are three main steps during the PL process. First, the electrons are excited to the conduction band from the top of the valence band. Next, some of the excited electrons are captured by different levels of sub-bands related to oxygen vacancies. These oxygen vacancies act as radiative centers. Finally, the trapped electrons in oxygen vacancies are recombined with the holes in the valence band to give rise to PL signals. Thus, the larger the concentration of oxygen vacancies, the stronger the PL signal. As shown in Fig. 3, the PL intensity of Ce-doped TiO_2 nanorods increases with Ce doping concentration which confirms that a large amount of oxygen vacancy has been introduced into the TiO_2 structures by Ce substitution. Moreover, the emission peaks' position of Ce-doped TiO_2 nanorods shows a blue-shift compared to that of the undoped TiO_2 nanorods, which is attributed to the shift of the optical bandgap in Ce-doped TiO_2 nanorods due to the Burstein–Moss effect. Therefore, Ce doping facilitates the formation of oxygen vacancies in doped TiO_2. In this way, two electrons released by formation of the oxygen vacancy play a significant role in increasing the electrical conductivity of the Ce-doped TiO_2.

In addition to oxygen vacancies and doping concentration, the electrical conductivity is significantly affected by the crystallinity of the prepared nanorods [26]. As can be seen from Table 2, when a small amount of cerium is incorporated into the TiO_2 lattice, the electrical conductivity starts to increase. With the substitution of cerium for titanium, the oxygen vacancy in the TiO_2 structure begins to increase and then two extra free electrons are created from each

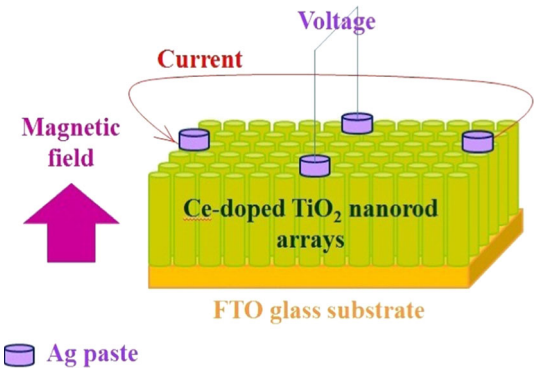

Figure 4 Schematic image of Hall effect measurement from the as-grown nanorod arrays.

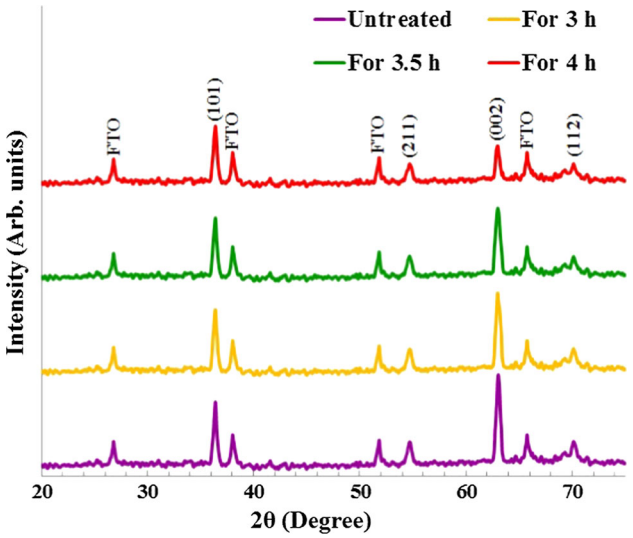

Figure 5 XRD patterns of 3 % Ce-doped TiO_2 nanorod arrays after hydrothermal treatment for different time durations.

oxygen vacancy. Due to this process, concentration of charge carriers increases with Ce content up to 3 % but further increase in the value of cerium content decreases the conductivity of the TiO_2 nanorods. The reduction of conductivity is attributed to the crystallinity deterioration of TiO_2 nanorods and appearance of an additional phase (see Fig. 1). Because of the limited solubility of Ce inside TiO_2 structure, at higher doping concentrations (>3 at %), some cerium atoms cannot occupy the correct places inside TiO_2 lattice and produce an extra phase (CeO_2) in the crystallite boundaries, which degrades the crystal structure of TiO_2 nanorods. Subsequently, the increase of cerium dopant concentration does not produce more charge carriers. Moreover, the mobility gradually decreases with the dopant content. In typical semiconductor materials, the decrease in Hall mobility is mainly due to different scattering mechanisms such as optical and acoustic phonon scattering mechanisms (also called lattice scattering), ionized and neutral impurity scattering, and grain boundary and defect scattering. In our study, the characterization of all samples has been carried out at room temperature in the same conditions. Thus, the phonon scattering does not contribute to the reduction of the Hall mobility. As mentioned above, with increasing Ce dopant content, the crystallinity of TiO_2 structure is deteriorated and the excess phase is formed (see Fig. 1). Therefore, the defect scattering originated from crystallinity deterioration of TiO_2 structure and the formation of doping oxide in the crystallite boundaries reduces the Hall mobility. These factors are also dominant in the reduction of electrical conductivity. The electrical conductivity (σ) is found to be influenced by the charge carrier concentration (n) and mobility of the charge carriers (μ), according to the formula $\sigma = \mu ne$ [47]. The results indicate that only appropriate amount of Ce can improve the electrical properties. The Hall effect measurement shows that the charge carrier concentration, mobility of the charge carriers, and the conductivity of the as-grown 3 % Ce-doped TiO_2 nanorods are about 6.6×10^{18} cm^{-3}, 4.6 cm^2 V^{-1} s^{-1}, and 4.8 S cm^{-1}, respectively. Schematic image of Hall effect measurement from the as-grown nanorod arrays is illustrated in Fig. 4.

A hydrothermal treatment was performed in the same Teflon-lined autoclave to convert the 3 % Ce-doped TiO_2 nanorods to nanotubes and the influence of hydrothermal treatment time on the morphology transformation was studied. The morphology change from the nanorods to the nanotubes takes place by the acid etching during hydrothermal treatment because the etching rate along (001) direction is faster than (101) direction [48, 49]. The preferential etching direction of the TiO_2 nanorods is elucidated by surface energy theory [50]. The surface energy is a main factor which determines the stability and reactivity of the surface [50]. In the rutile TiO_2 nanorods, the (101) and (001) surfaces have the lowest and highest surface energy values, respectively. Therefore, according to the surface energy theory, (101) facet is the most stable surface with lowest etching rate, whereas (001) facet is the most reactive surface with highest etching rate. Pan et al. and Zeng et al. showed that core and sidewall of the TiO_2 nanorods were composed of the (001) and (101) crystallites, respectively, and during

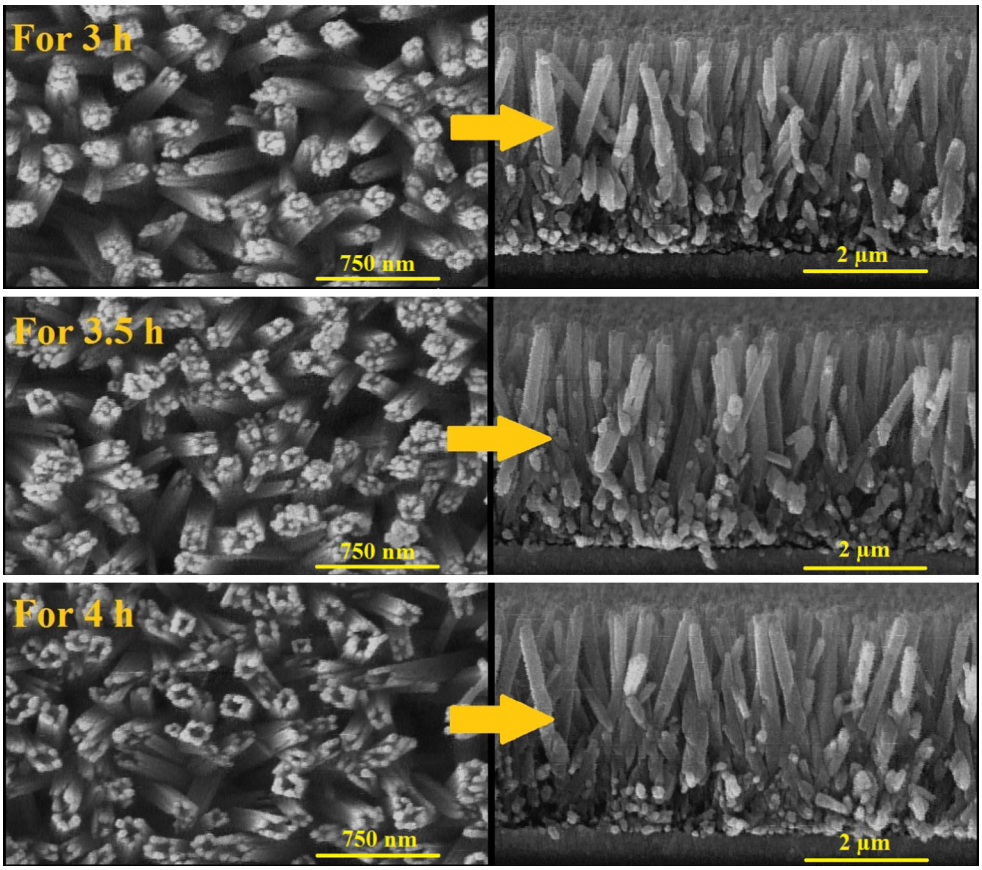

Figure 6 Top-view and cross-sectional FE-SEM images of 3 % Ce-doped TiO_2 nanorod arrays after hydrothermal treatment for different time durations.

the hydrothermal etching process, the (101) sidewalls undergo slower etching rate than the (001) cores [48, 49]. Comparison of XRD patterns of 3 % Ce-doped TiO_2 nanorods before and after hydrothermal treatment shows that the intensity of (002) peak suddenly decreases with hydrothermal treatment process (see Fig. 5). The etching occurs along [001] direction which covers both (001) and (002) facets. These results confirm that the etching rate along (001) direction of TiO_2 nanorods is faster than other directions. Our results are consistent with the recent reports for undoped 1D TiO_2 nanostructures [48, 49]. Figure 6 exhibits the FE-SEM images of 3 % Ce-doped TiO_2 nanorods after hydrothermal treatment for different time durations. During hydrothermal treatment at short time duration (<4 h), the TiO_2 nanorods are insufficiently etched and only a small portion of the nanorod tips is etched. When the hydrothermal treatment process is performed for 4 h, the central portion of the TiO_2 nanorods is successfully etched by the etching solution, and the as-grown vertically aligned 3 % Ce-doped TiO_2 nanorods are converted into ordered nanotubes. During hydrothermal treatment at the long time duration (>4 h), over-etching of the nanorods and the peeling-off of the nanorod arrays from the FTO substrate occurred.

The XRD pattern of the prepared nanoparticles (after annealing at 900 °C for 1 h) is shown in Fig. 7. For comparison, the XRD spectrum of undoped $CuCrO_2$ nanoparticles (prepared in a similar condition) is also presented. All peaks are indexed to a delafossite structure of $CuCrO_2$ and consistent with JCPDS Card No. 01-089-6744 [26]. The XRD results show that there is no extra peak corresponding to any impurity phase such as Mg and MgO, which indicates that magnesium ions have been homogeneously incorporated into the $CuCrO_2$ lattice during the preparation process. As can be seen from Fig. 7, the intensity of the diffraction peaks decreases after Mg-doping, indicating that Mg-doping can lead to reduction in the crystalline quality of $CuCrO_2$

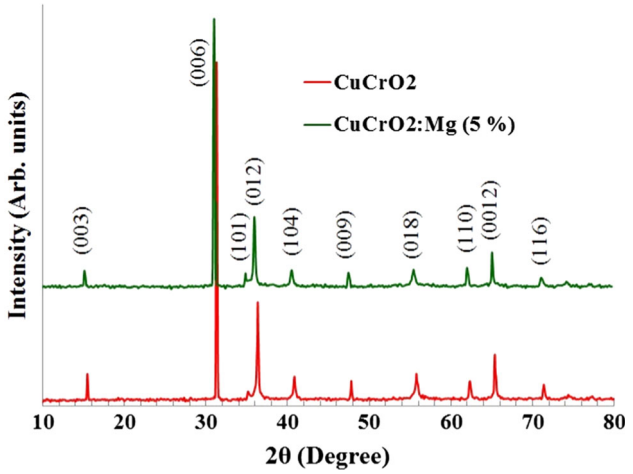

Figure 7 X-ray diffraction patterns of undoped and Mg-doped $CuCrO_2$ nanoparticles.

nanopowder. Furthermore, the addition of Mg dopant into $CuCrO_2$ structure increases the full-width at half-maximum of the XRD peaks and shifts their position toward lower angles [26]. The decrease in crystal quality may be due to the appearance of stress because of the difference in ionic size of Cr ($r_{Cr^{3+}} = 0.063$ nm) and Mg ($r_{Mg^{2+}} = 0.066$ nm). The theoretical calculations and experimental studies have shown that the conductivity of the $CuCrO_2$ structure is markedly increased when the small amount of divalent cations such as Ni^{2+}, Ca^{2+}, and Mg^{2+} are substituted in trivalent Cr^{3+} site due to the creation of free holes [51, 52]. This increase in p-type conductivity is linked to Cu^{1+}/Cu^{2+} hole mechanism [51]. In $CuCrO_2$ delafossite structure, the nominal valence of Cu and Cr is 1+ and 3+, respectively, and therefore three holes are required for charge compensation of the Cr vacancy. When one neutral Mg (with a valence of 2+) occupies a Cr site, the Mg donates two electrons to compensate holes generated by the Cr vacancy with one uncompensated hole. As a result, Cu^{1+} is oxidized to Cu^{2+}, creating a hole on Cu ion. This mechanism improves the p-type conductivity of the $CuCrO_2$ structure. The average crystallite size of the synthesized nanoparticles is determined from the most intense diffraction peak (006) using the Debye–Scherrer's equation—about 37.7 nm. According to this value, it is realized that the nanoparticles are relatively large and for a better penetration of the nanoparticles in the space between the nanorods, their size should be reduced. The typical FE-SEM and TEM images of the prepared 5 % Mg-doped $CuCrO_2$ nanoparticles after ball-milling for 5 h are illustrated in Fig. 8. This figure shows that the nanoparticles have spherical shape with uniform size which has been reduced to about 17 nm by milling.

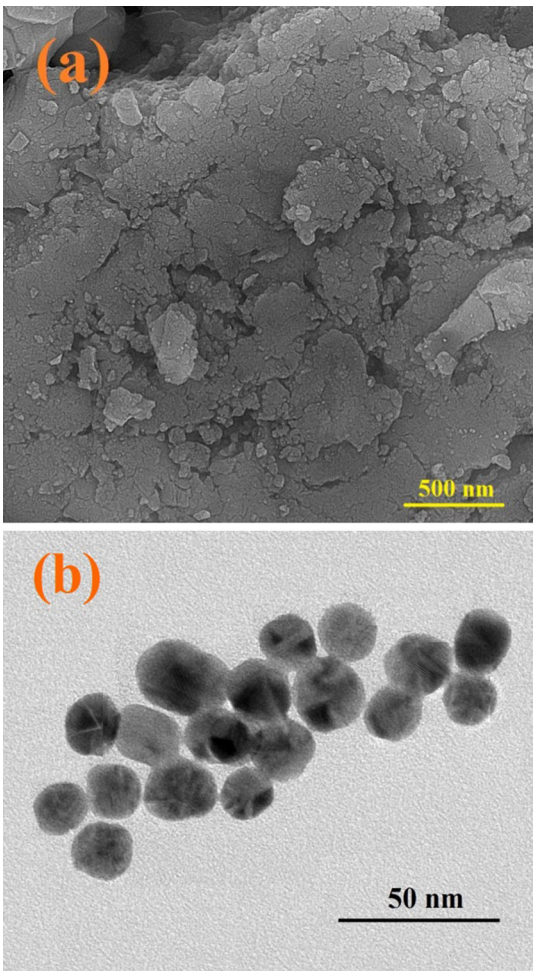

Figure 8 **a** FE-SEM and **b** TEM images of the synthesized Mg-doped $CuCrO_2$ nanoparticles after ball-milling for 5 h.

In order to investigate the effect of hydrothermal treatment on the performance of the solid-state DSSCs, different types of the hydrothermally treated nanorods were used as photoanode. This type of solid-state DSSC consists of dye-sensitized nanostructure metal oxide semiconductor (such as 1D TiO_2 nanostructure) on transparent conductive oxide glass, whose pore volume is filled with a transparent p-type semiconductor (such as $CuCrO_2$ nanoparticles). Schematic energy diagram of the solid-state DSSC components used in this study is shown in Fig. 9. Under sunlight irradiation, a thin layer of dye molecules at the interface between the n- and p-type

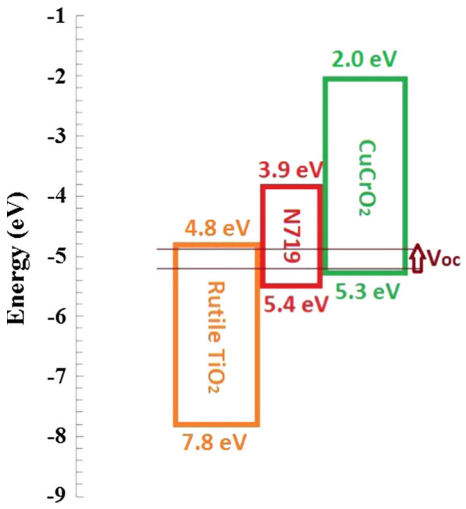

Figure 9 Schematic energy diagram of the solid-state DSSC device components used in this study. The mentioned values were extracted from ref. [53–55].

semiconductors injects electrons into the conduction band of the n-type semiconductor and then is regenerated by injecting holes into the valence band of the p-type semiconductor. The open-circuit voltage generated by this type of solid-state DSSC under illumination corresponds to the difference between the Fermi level of electrons in the n-type semiconductor and Fermi level of holes in the p-type semiconductor. Schematic images of the constructed solid-state DSSCs based on 1D nanostructures (nanorods and nanotubes) are displayed in Fig. 10a. A cross-sectional SEM image is also shown in Fig. 10b. It shows conductive glass substrates, nanorods, and nanoparticles which to some extent, penetrated into the space between nanorods. The photocurrent density–voltage (J–V) curves of DSSCs based on vertically aligned 3 % Ce-doped TiO_2 nanorods and

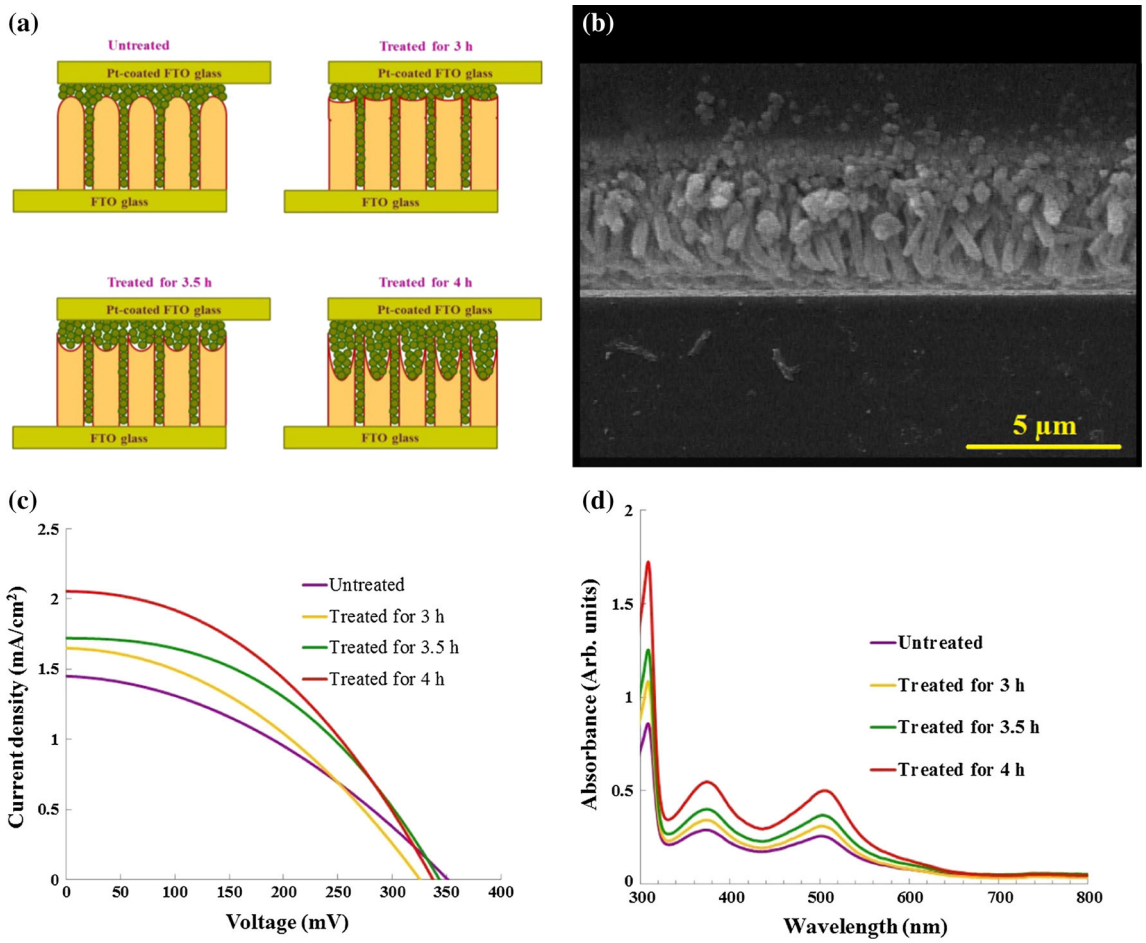

Figure 10 **a** Schematic images and **b** cross-sectional FE-SEM image of the constructed solid-state DSSCs based on 1D nanostructures, **c** current density–voltage characteristics of the solid-state DSSCs made from hydrothermally treated 3 % Ce-doped TiO_2 nanorods under simulated AM1.5G solar light (100 mW/cm^2), and **d** UV–Vis absorption spectra of the desorbed N719 dye molecules from the photoanodes.

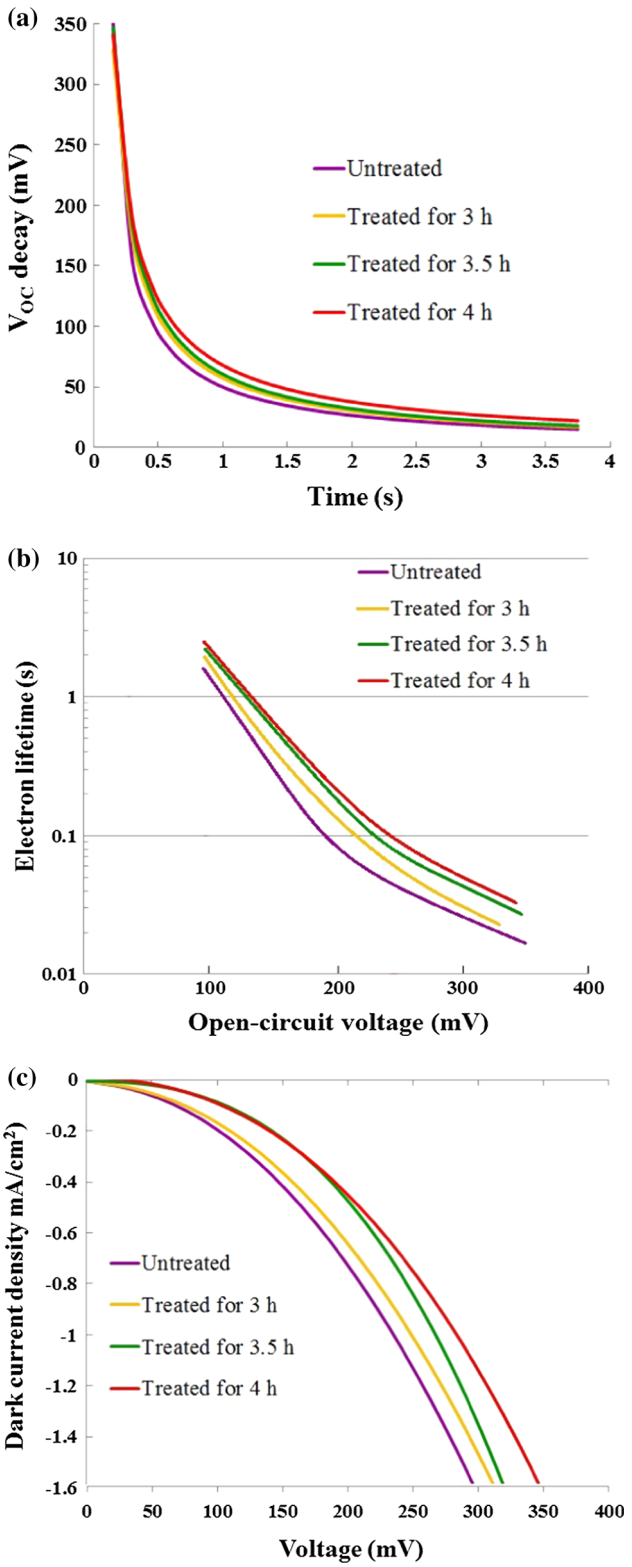

◀**Figure 11** **a** Open-circuit voltage decay for different solid-state DSSCs and **b** calculated electron lifetime as a function of open-circuit voltage. **c** Dark current density–voltage characteristics of the solid-state DSSCs made from hydrothermally treated 3 % Ce-doped TiO_2 nanorods.

nanotubes as photoanodes are shown in Fig. 10c. A short-circuit current density (J_{SC}) of 1.45 mA/cm^2, an open-circuit voltage (V_{OC}) of 351 mV, and an overall power conversion efficiency (PCE) of 0.18 % is obtained for the 3 % Ce-doped TiO_2 nanorod-based DSSC. After hydrothermal treatment for 3 and 3.5 h, the fabricated DSSCs with 3 % Ce-doped TiO_2 nanorod arrays show J_{SC} of 1.65 and 1.72 mA/cm^2, V_{OC} of 328 and 344 mV, and PCE of 0.21 and 0.23 %, respectively. Finally, obvious improvement in J_{SC}, 2.05 mA/cm^2, and the efficiency of 0.29 % is observed after hydrothermal treatment at 160 °C for 4 h. In comparison with untreated Ce-doped TiO_2 nanorod arrays, there is an observable enhancement in the short-circuit current density (from 1.45 to 2.05 mA/cm^2) as a result of 4 h hydrothermal treatment. Many parameters can influence the J_{SC} of the DSSCs, but in our case only one of them has significant effect. As can be seen from the FE-SEM images in Fig. 6, the tip of the nanorods is etched with hydrothermal treatment and then is converted to the nanotubes with the increasing treatment duration. The formation of large specific surface area for dye loading on the inner and outer sides of the nanotubes can be mentioned as the main reason for J_{SC} improvement. When more dye molecules are adsorbed on the surface of the photoanode, a large amount of electron–hole pair can be generated and participate in the photocurrent improvement. The UV–Vis absorption spectra verify that the amounts of adsorbed dye on the surface of the hydrothermally treated photoanodes are higher than that of untreated one (Fig. 10d).

Open-circuit photovoltage decay measurement is used to determine the electron lifetime in DSSCs. Zaban et al. clearly showed that the rate of open-circuit photovoltage decay is inversely proportional to the electron lifetime in DSSCs [56]. The relationship between the photovoltage decay and electron lifetime is given by

$$\tau_n = \frac{k_B T}{q}\left(\frac{dV_{oc}}{dt}\right)^{-1},$$

where k_B, T, and q are the Boltzmann constant, absolute temperature, and positive elementary charge, respectively. In order to measure the V_{OC}

decay, the simulated solar light is turned off and the decay of the photovoltage is recorded. Figure 11a shows the V_{OC} decay of the fabricated DSSCs. As can be seen, the decay of the photovoltage for hydrothermally treated photoanodes is slower than that of untreated one which indicates that the electron lifetime increases with hydrothermal treatment. The electron lifetimes determined from the V_{OC} decay measurements are about 15.4 ms for untreated photoanode and 20.7 ms (treated for 3 h), 25.9 ms (treated for 3.5 h), and 31.0 ms (treated for 4 h) for hydrothermally treated photoanodes at open-circuit voltage (see Fig. 11b). The highest lifetime of 31.0 ms has been recorded from the DSSC with 4 h hydrothermally treated Ce-doped TiO_2 nanorods (3 %), which suggests that the treatment of nanorods has an impressive influence on dye adsorption, electron generation, and electron transport through TiO_2 nanorods. The increase in the electron lifetime by hydrothermal treatment indicates that the number of defect sites and recombination centers has been reduced. This deduction could be confirmed by the dark J–V characteristics in Fig. 11c. The dark current in DSSCs is attributed to the recombination process at the photoanode/electrolyte interface. The 4 h hydrothermally treated Ce-doped TiO_2-based solid-state DSSC shows the lowest value of J_{SC}. The smallest dark current for this device specifies that the recombination at the TiO_2/Mg-doped $CuCrO_2$ interface has been suppressed and so, the electron transportation along conducting channels (hydrothermally treated nanorods) is more efficient.

To the best of our knowledge, these solar cells are the best reported to date. In 2007, the photovoltaic parameters of the solid-state DSSCs utilizing $CuAlO_2$ nanoparticles in TiO_2/N719 dye/$CuAlO_2$ structure have been reported by Bandara et al. with J_{SC} of 0.08 mA/cm^2 [57]. Lee et al. prepared n-TiO_2/p-NiO heterojunction electrodes for all-solid-state dye-sensitized solar cells with overall energy conversion efficiency of about 0.025 % [58]. Furthermore, Yuhas et al. have observed photovoltaic properties in FTO/ZnO nanowire/Cu_2O nanoparticles structure with energy conversion efficiency of about 0.053 % using a TiO_2 blocking layer [59]. We hope that our results will help to extend the potential applications of the delafossite-type semiconductors as new materials for all-oxide solid-state DSSCs in the future.

Conclusions

In summary, one-dimensional Ce-doped TiO_2 nanostructures were successfully grown on FTO glass by hydrothermal method. The influence of the Ce doping concentration on the structural properties and electrical characteristics of the TiO_2 nanorods were investigated. The highest electrical conductivity was obtained for 3 % Ce-doped TiO_2 nanorod arrays. The increase in the electrical conductivity is the result of the oxygen vacancy formation in TiO_2 nanostructures with Ce doping. Hydrothermal etching treatment for 4 h in acid solution created nanotubes from the nanorods. Sol–gel process was also employed to synthesize 5 % Mg-doped $CuCrO_2$ nanoparticles with p-type conductivity as solid-state electrolyte. The photovoltaic performance of the fabricated solid-state DSSCs with hydrothermally treated Ce-doped TiO_2 nanorods were improved due to the large specific surface area. The dye-loading measurement confirmed that the amount of adsorbed dye on the surface of hydrothermally treated photoanodes is higher than that of untreated one. By the techniques employed in this study, the highest efficiency of about 0.3 % was obtained for the solid-state DSSCs based on delafossite nanoparticles.

Acknowledgements

We gratefully acknowledge financial support from the Iran National Science Foundation (INSF), under Grant number 93034818.

References

[1] Vu THT, Au HT, Tran LT, Nguyen TMT, Tran TTT, Pham MT, Do MH, Nguyen DL (2014) Synthesis of titanium dioxide nanotubes via one-step dynamic hydrothermal process. J Mater Sci 49:5617–5625

[2] Rahmani N, Dariani RS, Rajabi M (2016) A proposed mechanism for investigating the effect of porous silicon buffer layer on TiO_2 nanorods growth. Appl Surf Sci 366:359–364

[3] Yildizhan MM, Sturm S, Gulgun MA (2016) Structural and electronic modifications on TiO_2 anatase by Li, K or Nb doping below and above the solubility limit. J Mater Sci 51:5912–5923

[4] Meng L, Ma A, Ying P, Feng Z, Li C (2011) Sputtered highly ordered TiO_2 nanorod arrays and their applications as

the electrode in dye-sensitized solar cells. J Nanosci Nanotechnol 11:929–934

[5] Zhao Y, Gu X, Qiang Y (2012) Influence of growth time and annealing on rutile TiO_2 single-crystal nanorod arrays synthesized by hydrothermal method in dye-sensitized solar cells. Thin Solid Films 520:2814–2818

[6] Wei Z, Liu Y, Wang H, Mei Z, Ye J, Wen X, Gu L, Xie Y (2012) A gas-solid reaction growth of dense TiO_2 nanowire arrays on Ti foils at ambient atmosphere. J Nanosci Nanotechnol 12:316–323

[7] Shankar K, Mor GK, Prakasam HE, Yoriya S, Paulose M, Varghese OK, Grimes CA (2007) Highly-ordered TiO_2 nanotube arrays up to 220 μm in length: use in water photoelectrolysis and dye-sensitized solar cells. Nanotechnology 18:065707–065787

[8] Foong TRB, Shen Y, Hu X, Sellinger A (2010) Template-directed liquid ALD growth of TiO2 nanotube arrays: properties and potential in photovoltaic devices. Adv Funct Mater 20:1390–1396

[9] Chen RS, Chen CA, Wang WC, Tsai HY, Huang YS (2011) Transport properties in single-crystalline rutile TiO_2 nanorods. Appl Phys Lett 99:222107–222109

[10] Wang HE, Chen Z, Leung YH, Luan C, Liu C, Tang Y, Yan C, Zhang W, Zapien JA, Bello I, Lee ST (2010) Hydrothermal synthesis of ordered single-crystalline rutile TiO_2 nanorod arrays on different substrates. Appl Phys Lett 96:263104–263106

[11] Ameen S, Akhtar MS, Kim YS, Shin HS (2012) Controlled synthesis and photoelectrochemical properties of highly ordered TiO_2 nanorods. RSC Adv 2:4807–4813

[12] Liu B, Aydil ES (2009) Growth of oriented single-crystalline rutile TiO_2 nanorods on transparent conducting substrates for dye-sensitized solar cells. J Am Chem Soc 131:3985–3990

[13] Al-bahrani MR, Liu L, Ahmad W, Tao J, Tu F, Cheng Z, Gao Y (2015) NiO-NF/MWCNT nanocomposite catalyst as a counter electrode for high performance dye-sensitized solar cells. Appl Surf Sci 331:333–338

[14] Wang W, Chen J, Luo J, Zhang Y, Gao L, Liu Y, Sun J (2015) Effects of low pressure plasma treatments on DSSCs based on rutile TiO_2 array photoanodes. Appl Surf Sci 324:143–151

[15] Mathew S, Yella A, Gao P, Humphry-Baker R, Curchod BFE, Ashari-Astani N, Tavernelli I, Rothlisberger U, Nazeeruddin MK, Gratzel M (2014) Dye-sensitized solar cells with 13% efficiency achieved through the molecular engineering of porphyrin sensitizers. Nat Chem 6:242–247

[16] Jiang X, Karlsson KM, Gabrielsson E, Johansson EMJ, Quintana M, Karlsson M, Sun L, Boschloo G, Hagfeldt A (2011) Highly efficient solid-state dye-sensitized solar cells based on triphenylamine dyes. Adv Funct Mater 21:2944–2952

[17] Chen X, Tang Q, He B, Chen H (2015) Graphene-incorporated quasi-solid-state dye-sensitized solar cells. RSC Adv 5:43402–43407

[18] Dkhissi D, Huang F, Cheng YB, Caruso RA (2014) Quasi-solid-state dye-sensitized solar cells on plastic substrates. J Phys Chem C 118:16366–16374

[19] Seidalilir Z, Malekfar R, Wu HP, Shiu JW, Diau EWG (2015) High-performance and stable gel-state dye-sensitized solar cells using anodic TiO_2 nanotube arrays and polymer-based gel electrolytes. Appl Mater Interfaces 7:12731–12739

[20] Nejati S, Lau KKS (2011) Pore filling of nanostructured electrodes in dye sensitized solar cells by initiated chemical vapor deposition. Nano Lett 11:419–423

[21] Song MY, Ahn YR, Jo SM, Kim DY (2005) TiO_2 single-crystalline nanorod electrode for quasi-solid-state dye-sensitized solar cells. Appl Phys Lett 87:113113–113115

[22] Flores IC, Freitas JND, Longo C, Paoli MAD, Winnischofer H, Nogueira AF (2007) Dye-sensitized solar cells based on TiO_2 nanotubes and a solid-state electrolyte. J Photochem Photobiol, A 189:153–160

[23] Xu C, Wu J, Desai UV, Gao D (2012) High-efficiency solid-state dye-sensitized solar cells based on TiO_2-coated ZnO nanowire arrays. Nano Lett 12:2420–2424

[24] Roh DK, Chi WS, Jeon H, Kim SJ, Kim JH (2014) High efficiency solid-state dye-sensitized solar cells assembled with hierarchical anatase pine tree-like TiO2 nanotubes. Adv Funct Mater 22:379–386

[25] Wang M, Bai J, Formal FL, Moon SJ, Cevey-Ha L, Humphry-Baker R, Gratzel C, Zakeeruddin SM, Gratzel M (2012) Solid-state dye-sensitized solar cells using ordered TiO_2 nanorods on transparent conductive oxide as photoanodes. J Phys Chem C 116:3266–3273

[26] Asemi M, Ghanaatshoar M (2016) Conductivity improvement of $CuCrO_2$ nanoparticles by Zn doping and their application in solid-state dye-sensitized solar cells. Ceram Int 42:6664–6672

[27] Hwang D, Jo SM, Kim DY, Armel V, Farlane DRM, Jang SY (2011) High-efficiency, solid-state, dye-sensitized solar cells using hierarchically structured TiO_2 nanofibers. ACS Appl Mater Interfaces 3:1521–1527

[28] He C, Zheng Z, Tang H, Zhao L, Lu F (2009) Electrochemical impedance spectroscopy characterization of electron transport and recombination in ZnO nanorod dye-sensitized solar cells. J Phys Chem C 113:10322–10325

[29] Desai UV, Xu C, Wu J, Gao D (2012) Solid-state dye-sensitized solar cells based on ordered ZnO nanowire arrays. Nanotechnology 23:205401–205407

[30] Chen SW, Lee JM, Lu KT, Pao CW, Lee JF, Chan TS, Chen JM (2010) Band-gap narrowing of TiO_2 doped with Ce probed with x-ray absorption spectroscopy. Appl Phys Lett 97:012104–012106

[31] Iwaszuk A, Nolan M (2011) Electronic structure and reactivity of Ce-and Zr-doped TiO_2: assessing the reliability of density functional theory approaches. J Phys Chem C 115:12995–13007

[32] Albuquerque AR, Bruix A, Santos IMG, Sambrano JR, Illas F (2014) DFT study on Ce-doped anatase TiO_2: nature of Ce^{3+} and Ti^{3+} centers triggered by oxygen vacancy formation. J Phys Chem C 118:9677–9689

[33] Nowotny MK, Bak T, Nowotny J (2006) Electrical properties and defect chemistry of TiO_2 single crystal. I. electrical conductivity. J Phys Chem B 110:16270–16282

[34] Janotti A, Varley JB, Rinke P, Umezawa N, Kresse G, Walle CGW (2010) Hybrid functional studies of the oxygen vacancy in TiO_2. Phys Rev B 81:085212–085218

[35] Ye M, Zheng D, Wang M, Chen C, Liao W, Lin C, Lin Z (2014) Hierarchically structured microspheres for high-efficiency rutile TiO_2-based dye-sensitized solar cells. Appl Mater Interfaces 6:2893–2901

[36] Liao Y, Que W, Jia Q, He Y, Zhang J, Zhong P (2012) Controllable synthesis of brookite/anatase/rutile TiO_2 nanocomposites and single-crystalline rutile nanorods array. J Mater Chem 22:7937–7944

[37] Abd El-Hafiz DR, Ebiad MA, Elsalamony RA, Mohamed LS (2015) Highly stable nano Ce-La catalyst for hydrogen production from bio-ethanol. RSC Adv 5:4292–4303

[38] Xiao G, Huang X, Liao X, Shi B (2013) One-pot facile synthesis of cerium-doped TiO_2 mesoporous nanofibers using collagen fiber as the biotemplate and its application in visible light photocatalysis. J Phys Chem C 117:9739–9746

[39] Hamedani HA, Allam NK, El-Sayed MA, Khaleel MA, Garmestani H, Alamgir FM (2014) An experimental insight into the structural and electronic characteristics of strontium-doped titanium dioxide nanotube arrays. Adv Funct Mater 24:6783–6796

[40] Asemi M, Ghanaatshoar M (2014) Preparation of $CuCrO_2$ nanoparticles with narrow size distribution by sol-gel method. J Sol-Gel Sci Technol 70:416–421

[41] Xiao G, Huang X, Liao X, Shi B (2013) One-pot facile synthesis of cerium-doped TiO_2 mesoporous nanofibers using collagen fiber as the biotemplate and its application in visible light photocatalysis. J Phys Chem C 117:9739–9746

[42] Worayingyong A, Sang-urai S, Smith MF, Maensiri S, Seraphin S (2014) Effects of cerium dopant concentration on structural properties and photocatalytic activity of electrospun Ce-doped TiO_2 nanofibers. Appl Phys A 117:1191–1201

[43] Xiao S, Zhao L, Lian J (2014) enhanced photocatalytic performance of supported Fe doped ZnO nanorod arrays prepared by wet chemical method. Catal Lett 144:347–354

[44] Liang Z, Cui H, Wang K, Yang P, Zhang L, Mai W, Wang CX, Liu P (2012) Morphology-controllable ZnO nanotubes and nanowires: synthesis, growth mechanism and hydrophobic property. CrystEngComm 14:1723–1728

[45] Lu X, Mou X, Wu J, Zhang D, Zhang L, Huang F, Xu F, Huang S (2010) Improved-performance dye-sensitized solar cells using Nb-doped TiO2 electrodes: efficient electron injection and transfer. Adv Funct Mater 20:509–515

[46] Wang C, Shi H, Li Y (2012) Synthesis and characterization of natural zeolite supported Cr-doped TiO_2 photocatalysts. Appl Surf Sci 258:4328–4333

[47] Diaz EC, Camacho JM, Duarte-Moller A, Castro-Rodriguez R, Bartolo-Perez P (2010) Influence of the oxygen pressure on the physical properties of the pulsed-laser deposited Te doped SnO_2 thin films. J. Alloys Compd 508:342–347

[48] Pan L, Huang H, Lim CK, Hong QY, Ooi MST, Tan K (2013) TiO_2 rutile–anatase core–shell nanorod and nanotube arrays for photocatalytic applications. RSC Adv 3:3566–3571

[49] Zeng R, Li K, Sheng X, Chen L, Zhang H, Feng X (2016) A room temperature approach for the fabrication of aligned TiO_2 nanotube arrays on transparent conductive substrates. Chem Commun 52:4045–4048

[50] Yang HG, Sun CH, Qiao SZ, Zou J, Liu G, Smith SC, Cheng HM, Lu GQ (2008) Anatase TiO_2 single crystals with a large percentage of reactive facets. Nature 453:638–641

[51] Scanlon DO, Watson GW (2011) Understanding the p-type defect chemistry of $CuCrO_2$. J Mater Chem 21:3655–3663

[52] Barnabe A, Thimont Y, Lalanne M, Presmanes L, Tailhades P (2015) P-Type conducting transparent characteristics of delafossite Mg-doped $CuCrO_2$ thin films prepared by RF-sputtering. J Mater Chem C 3:6012–6024

[53] Scanlon DO, Dunnill CW, Buckeridge J, Shevlin SA, Logsdail AJ, Woodley SM, Catlow CRA, Powell MJ, Palgrave RG, Parkin IP, Watson GW, Kea TW, Sherwood P, Walsh A, Sokol AA (2013) Band alignment of rutile and anatase TiO_2. Nat Mater 12:798–801

[54] Wei L, Yang Y, Fan R, Wang P, Li L, Yu J, Yang B, Cao W (2013) Enhance the performance of dye-sensitized solar cells by co-sensitization of 2,6-bis(iminoalkyl)pyridine and N719. RSC Adv 3:25908–25916

[55] Powar S, Xiong D, Daeneke T, Ma MT, Gupta A, Lee GP, Makuta S, Tachibana Y, Chen W, Spiccia L, Cheng YB, Gotz G, Bauerle P, Bach U (2014) Improved photovoltages for p-type dye-sensitized solar cells using $CuCrO_2$ nanoparticles. J Phys Chem C 118:16375–16379

[56] Zaban A, Greenshtein M, Bisquert J (2003) Determination of the electron lifetime in nanocrystalline dye solar cells by open-circuit voltage decay measurements. ChemPhysChem 4:859–864

[57] Bandara J, Yasomanee JP (2007) P-type oxide semiconductors as hole collectors in dye-sensitized solid-state solar cells. Semicond Sci Technol 22:20–24

[58] Lee YM, Lai CH (2009) Preparation and characterization of solid n-TiO_2/p-NiO hetrojunction electrodes for all-solid-state dye-sensitized solar cell. Solid State Electron 53:1116–1125

[59] Yuhas BD, Yang P (2009) Nanowire-based all-oxide solar cells. J Am Chem Soc 131:3756–3761